

COSMOLOGICAL IMPLICATIONS OF THE BIMA 30 GHz
SUNYAEV-ZEL'DOVICH EFFECT GALAXY CLUSTER SURVEY

YEN-TING LIN¹ AND JOSEPH J. MOHR^{1,2}

Submitted to ApJ June 28, 2002

ABSTRACT

We explore the cosmological implications of 7 deep survey fields observed at the Berkeley-Illinois-Maryland Association (BIMA) Array with 30 GHz receivers. These observations probe the Cosmic Microwave Background anisotropy on scales corresponding to $l \sim 5500$, and an earlier analysis of these data detected no galaxy clusters. We use numerical cluster simulations and mock observations to characterize the cluster detection efficiency for each of the BIMA fields. With these detection efficiencies we derive constraints on the cosmological parameters Ω_M and σ_8 , ruling out those models which overproduce galaxy clusters. Using only these seven BIMA fields, we calculate a 2σ upper limit of $\sigma_8 < 1.00 \Omega_M^{-0.43\Omega_M - 0.22}$ for flat models with $0.1 \leq \Omega_M \leq 1$. When the power spectrum of density fluctuations is COBE normalized, we find $\Omega_M < 0.63$ at 95% confidence level for flat models. This constraint includes our estimate of the large uncertainties in the SZE flux–virial mass relationship as well as published uncertainties in the Hubble parameter, the COBE power spectrum normalization and the primordial power spectrum index. In addition, we account for the effects of sample variance. Thus, we conclude that the non-detections are to be expected in a low Ω_M universe, given the sensitivity and solid angle of the deepest SZE survey to date.

Subject headings: cosmology: observation – galaxies: clusters – cosmic microwave background

1. INTRODUCTION

Cosmic microwave background (CMB) images provide information about the presence of galaxy clusters over a wide range of redshift, because galaxy clusters leave signatures in the CMB through the so-called Sunyaev-Zel'dovich effect (SZE; Sunyaev & Zeldovich 1970; Sunyaev & Zel'dovich 1972). The SZE is produced by inverse Compton interactions between the CMB photons and the hot electrons ($k_B T_e \sim 1$ keV, see §2.1) in the intracluster medium. The intracluster medium is shocked and heated in the process of cluster formation. The net result in the SZE is a transfer of energy from the electron population to the CMB photons, leading to a distortion in the CMB spectrum. The thermal SZE signature of a cluster in 1 cm (~ 30 GHz) observations is a reduction in the CMB brightness. On angular scales of $\sim 5'$ and smaller the thermal SZE contribution to the CMB anisotropy can dominate that of the primary CMB anisotropy (Holder & Carlstrom 1999; Holzapfel et al. 2000a; Hu & Dodelson 2001; Springel et al. 2001).

Here we discuss the cosmological implications of 7 deep survey fields observed at the Berkeley–Illinois–Maryland Association (BIMA) array with the 30 GHz receivers (Carlstrom et al. 1996; Holzapfel et al. 2000a). The observations were made during 1997 and 1998, in a compact configuration at 28.5 GHz, providing a Gaussian primary beam with FWHM $\sim 6'.6$. This survey, originally planned to probe the CMB anisotropy on arcminute scales $l \sim 5500$ (corresponding to angular size $\sim 2'$), provides relatively large sky coverage (~ 250 arcminute²) for an arcminute-scale anisotropy experiment. These observations have been used to place an upper limit on small

scale CMB anisotropy (Holzapfel et al. 2000a). Continued observations on these and additional fields has led to a detection of anisotropy with flat band power at the level $Q_{flat} = 6.1_{-4.8}^{+2.8} \mu K$, where uncertainties describe 68% confidence regions (Dawson et al. 2001, see also Dawson et al. 2002). In addition, no galaxy cluster detections were reported, which is interesting because of the sensitivity of SZE surveys to high redshift clusters. In the currently favored cosmology, these seven fields sweep out as much comoving volume to $z \sim 2$ as a 130 deg² local survey sweeps out to $z \sim 0.1$.

In principle, cluster surveys constrain cosmological parameters through the effects those parameters have on the volume surveyed per solid angle and the evolution of cluster abundance (e.g. Haiman et al. 2001; Holder et al. 2001; Mohr 2001). In this analysis we focus on the lack of clusters in these deep '97 and '98 BIMA fields. A less sensitive, earlier survey with the Australian Telescope Compact Array also provided upper limits on the CMB anisotropy on similarly small scales (Subrahmanyam et al. 2000). An analysis of the cosmological implications of that survey, which relied on the assumption that the dominant source of anisotropy on arcminute scales is the thermal SZE from clusters, concluded that a low- Ω_M universe is preferred (Majumdar & Subrahmanyam 2000).

An analysis of this BIMA survey allows us to rule out cosmological models which produce too many clusters. The expected number of detected clusters in a survey is

$$\langle N \rangle = \int d\Omega \int dV \int_0^\infty dM f(M) \frac{dn}{dM}(M, z), \quad (1)$$

where $(dn/dM)dM$ is the comoving number density of objects of mass between M and $M + dM$, $f(M)$ is the detection efficiency ($0 \leq f(M) \leq 1$), which takes into account

¹Department of Astronomy, University of Illinois; Urbana, IL 61801; ylin2@astro.uiuc.edu

²Department of Physics, University of Illinois; Urbana, IL 61801; jmohr@uiuc.edu

the fact that only clusters with masses above some mass limits can be detected. The first integral is over the solid angle of the survey, the second integral is over the redshift, and the third integral sums over the portion of the cluster mass function to which our survey is sensitive. In addition to its dependence on mass, the detection efficiency $f(M)$ depends on the sky position (α, δ) , the redshift z and cosmological parameters such as H_0 , Ω_M and Ω_Λ .

Cosmological constraints come through comparison of the observed and the expected number of clusters. In the BIMA survey no clusters were detected; assuming Poisson statistics, the probability P of observing 0 clusters is $P(0|N) = e^{-N}$. Using this approach we explore the parameter space spanned by Ω_M and σ_8 , checking the consistency of these cosmological models. We also consider the uncertainties in the cluster detection efficiency $f(M)$, Hubble parameter, COBE power spectrum normalization, power spectrum index and the effects of sample variance.

This paper is organized as follows: in §2 we present a general description of interferometric SZE observations, describe the BIMA survey data, and determine the survey detection efficiency via mock observations of hydrodynamic cluster simulations. We discuss the ingredients needed for the calculations of cluster abundance in §3. The cosmological constraints and a discussion on effects of systematic errors appear in §4. We present a summary and discussion on prospects of future interferometry SZE observations in §5. We discuss the H_0 scaling of interferometric SZE observations in the Appendix.

2. SURVEY SENSITIVITY TO CLUSTERS

The expected number of detected clusters in each cosmology depends sensitively on the detection efficiency function $f(M)$, characterized by a limiting detectable mass M_{lim} at which $f(M_{lim}) = 0.5$. We determine the detection efficiency by conducting mock observations of hydrodynamical cluster simulations using the exact characteristics of the real BIMA observations. In this section, we first discuss the interferometric observations of the cluster SZE, then describe the BIMA data, and provide a detailed description of the determination of the detection efficiency.

2.1. Interferometric SZE Observations of Clusters

Interferometric observations of cluster SZE have greatly advanced in the past decade (Carlstrom et al. 2000). Interferometers can observe a wide range of angular scales simultaneously, reduce possible confusion due to radio point sources toward galaxy clusters, and generate high-fidelity SZE images.

Interferometers measure the visibility $V_\lambda(u, v)$, whose Fourier transform pair, the specific intensity $I_\lambda(\theta_x, \theta_y)$, is directly proportional to the Compton $y(\theta_x, \theta_y)$ distribution of the cluster. Along any line of sight,

$$y = \sigma_T \int dl n_e \frac{k_B T_e}{m_e c^2}, \quad (2)$$

where σ_T is the Thomson scattering cross-section, n_e is the electron number density, m_e is the electron rest mass, c is the speed of light, k_B is the Boltzmann constant and T_e is the electron temperature. The SZE temperature decrement is then $\Delta T = g(x) y T_{CMB}$, where $x = h\nu/k_B T_{CMB}$ is the dimensionless frequency, $T_{CMB} = 2.728$ K (Fixsen

et al. 1996) is the mean cosmic microwave background temperature, and, within the Kompaneets approximation, $g(x) = x(e^x + 1)/(e^x - 1) - 4$ is the amplitude of the spectral distortion. In the Rayleigh–Jeans regime ($x \ll 1$) $g(x) \approx -2$, and at the central frequency of these BIMA observations, $\nu = 28.5$ GHz, $g(x) = -1.9583$. We convert this decrement distribution $\Delta T(\theta_x, \theta_y)$ into specific intensity $I_\lambda(\theta_x, \theta_y)$ using

$$I_\lambda(\theta_x, \theta_y) = 2 \frac{k_B \Delta T(\theta_x, \theta_y)}{\lambda^2}. \quad (3)$$

where λ is the wavelength of observation. The visibility $V_\lambda(u, v)$ then is the Fourier transform of the intensity distribution or image $I_\lambda(\theta_x, \theta_y)$ multiplied by the telescope primary beam $B(\theta_x, \theta_y)$,

$$\begin{aligned} V_\lambda(u, v) &= \iint d\theta_x d\theta_y I_\lambda B e^{-2\pi i(u\theta_x + v\theta_y)} \\ &= \tilde{I}_\lambda \otimes \tilde{B}, \end{aligned} \quad (4)$$

where \tilde{I}_λ and \tilde{B} are the Fourier transforms of I_λ and B , respectively, and \otimes denotes convolution. For this analysis, we take the BIMA primary beam to be a Gaussian with FWHM = 6'.33; therefore \tilde{B} is also a Gaussian. Because $V_\lambda(0) = \int d^2\theta I_\lambda B$, the overall normalization of the measured visibilities in the case that the cluster lies well within the BIMA primary beam (i.e. $B \simeq 1$) and observation frequencies are in the Rayleigh–Jeans limit is directly related to the cluster flux within the virial region:

$$V_\lambda(0) \xrightarrow{B \simeq 1} S_{200} = \frac{-4 \sigma_T k_B^2 T_{CMB}}{\lambda^2 m_e c^2 d_A(z)^2} \langle T_e \rangle \frac{f_{ICM} M_{200}}{\mu_e m_p} \quad (5)$$

where $\langle T_e \rangle$ is the electron density weighted mean temperature of the cluster, d_A is the angular diameter distance, μ_e is the mean molecular weight per electron, m_p is the rest mass of proton, f_{ICM} is the ratio of intracluster gas mass to binding mass, and $M_{200} \equiv 4\pi/3 r_{200}^3 \times 200\rho_c$ is a measure of total cluster binding mass, within which the mean overdensity is 200 times of the critical density ρ_c . This expression also defines the virial radius r_{200} . Note that Eqn 5 does not account for any SZE flux contribution from outside the cluster virial region. Also notice that, the only cosmology-dependence of the flux comes from d_A .

To examine the sensitivity of cluster visibilities to cluster size and morphology, we adopt a cluster temperature decrement model. We use the spherical β model (Cavaliere & Fusco-Femiano 1978), $\Delta T(\theta) = \Delta T_0 (1 + (\theta/\theta_c)^2)^{(1-3\beta)/2}$, where ΔT_0 is the temperature decrement toward the cluster center, and $\theta_c = r_c/d_A$ is the angular core radius. Comparison of this model with our simulated cluster ΔT maps indicates that it provides a reasonable description of clusters with $\langle \beta \rangle \simeq 1.1$. For $\beta = 4/3$ in the case where the primary beam is larger than the cluster (i.e. $B \simeq 1$), the visibility and the SZE flux within the virial radius is related by:

$$V_\lambda(q) = \frac{S_{200}}{\Theta} e^{-2\pi\theta_c q} \quad (6)$$

where $q = (u^2 + v^2)^{1/2}$, $\Theta = 1 - (1 + (\theta_{200}/\theta_c)^2)^{-1/2}$ is the fraction of the total cluster flux that lies within $\theta_{200} = r_{200}/d_A$, the angular extent of the virial radius.

In general, all interferometers are incapable of measuring $V_\lambda(0)$ directly, and the BIMA interferometer is constrained to measure cluster visibilities at $q > D/\lambda \sim 600$

(D is the telescope diameter). Eqn 6 shows clear that the shape, the size and the total integrated flux from the cluster affect the measured visibilities. An accurate determination of the survey mass selection function $f(M)$ requires knowledge of cluster morphologies. This fact also means that the simple Hubble parameter h scaling that one derives by assuming that the total cluster SZE flux is the only important variable is incorrect. We discuss this point more in the Appendix. In future surveys it will be possible to use observed cluster visibilities along with independent mass measurements to accurately determine the survey selection function. In the current work we use hydrodynamical simulations of clusters to determine the survey selection.

2.2. The BIMA Deep Survey Data

The data are from a study of the CMB anisotropy on arcminute angular scales (Holzapfel et al. 2000a). Fields were chosen to contain no known, bright radio point sources. The observations were made with the BIMA array with a central frequency of 28.5 GHz and ~ 800 MHz of bandwidth. The receivers are based on low-noise, high electron mobility transistor (HEMT) amplifiers, and are sensitive only to right-circularly polarized radiation. More details on the receivers are given in Carlstrom et al. (1996). Supporting observations were done with the Owens Valley Radio Observatory (OVRO) for aid in the detection and removal of radio point sources in two of the fields.

Of the seven BIMA fields included in this analysis, three were observed in 1997 (the first 3 in Table 1), and the rest were observed in 1998. Additional observations of these and other CMB fields have since been obtained (Dawson et al. 2001, 2002). Previous observations by other teams (Jones et al. 1997; Richards et al. 1997) suggested temperature decrements with marginal significance in two of the 1997 fields. However, the higher sensitivity BIMA observations failed to confirm these detections. The four 1998 fields are evenly distributed in right ascension, in regions of low IR dust emission that are free of bright optical and X-ray sources. Additional details of these fields are summarized in Table 1 and in Holzapfel et al. (2000a).

For the purposes of our analysis, only the list of visibility measurement positions (u_i, v_i) and uncertainties σ_i^2 are required. We perform no further analysis of the actual observations; however, we describe some general details of the analysis from Holzapfel et al. (2000a). To remove point sources from the data, a long baseline ($> 2.4 k\lambda$) map was made for each field; five point sources were found in the seven fields (but see Dawson et al. 2002). Identified point sources were removed from the visibility data by subtracting the best fit model of the point source, modulated by the primary beam.

The processed data were analyzed by a Bayesian maximum likelihood method. A likelihood function was constructed from the visibility correlation matrix. With this technique the consistency of a theory on CMB fluctuations could be obtained by comparison to the data. Because the fields are independent, the total probability is the product of that from individual fields. The joint likelihood for the combined data is expressed in terms of the flat-band power amplitude: $Q_{flat} \equiv 5 C_l l(l+1)/24\pi < 14.1 \mu\text{K}$ at 95% confidence, where C_l is the amplitude of the CMB

angular power spectrum of mode l .

Holzapfel et al. (2000a) found that, of the seven fields, two show excess power ($Q_{flat} > 0$); however, the confidence of a non-trivial signal is only 44% for the joint likelihood analysis, and each of the fields is consistent with no signal at 95% confidence level. Based on this information together with the argument that the thermal SZE is the dominant source of anisotropy on this angular scale, we infer that no galaxy clusters were detected at or above the 95% confidence limit. This inference is uncertain, because quantitative results of a sophisticated search for extended, negative sources (i.e. cluster SZE signatures) have not been reported by the authors in the three manuscripts that have appeared to date. Thus, we also examine the sensitivity of our limits on Ω_M to the numerical significance we ascribe to the non-detections (see §4.3.4).

2.3. Determining the Detection Efficiency

The cluster mass M is the single most important factor in interferometric cluster SZE observations (e.g. Holder et al. 2000). From Eqn 5 we expect a direct correspondence between the flux from a cluster and its mass. In an ideal flux limited survey, this naturally leads to the functional form of the detection efficiency which is a step function: $f(M \geq M_{lim}) = 1$ and $f(M < M_{lim}) = 0$, where M_{lim} is the cluster mass that corresponds to the minimum detectable flux of the survey. However, we expect scatter about the total SZE flux–virial mass relation, because of departures from equilibrium and variations in cluster morphology at a fixed mass. These morphological variations are particularly important in an interferometric survey, where the observed visibility has direct sensitivity to cluster shape and size. Therefore, we use an $f(M)$, that varies continuously from $f(M) = 0$ for $M \ll M_{lim}$ to $f(M) = 1$ for $M \gg M_{lim}$.

The method is that given a set of cosmological parameters (here H_0 , Ω_M and Ω_Λ), a redshift, and a position on the sky (α, δ) , we simulate observations and detections of an ensemble of clusters with a large range of masses. These mock interferometric SZE observations have characteristics such as sensitivity, u - v coverage, and primary beam identical to those carried out in the BIMA survey. We then choose the detection efficiency M_{lim} so that it reflects the mass of clusters detected at 95% confidence.

In practice, we account for the cosmological sensitivity of the limiting mass through the dependence of the cluster flux on the angular diameter distance d_A (Eqn 5). To determine the coordinate dependence of M_{lim} for each BIMA field, we carry out sets of mock observations at 8 off-axis angles θ in the range $0' \leq \theta \leq 3'.5$ and 6 azimuthal angles ϕ (although we expect azimuthal symmetry). At each of these field positions (θ, ϕ) , we examine the detectability of 48 simulated clusters (observed along 3 orthogonal axes, §2.3.1) at redshift $z = 0.5$, where the cluster angular diameter distance is determined within a fiducial cosmology. To determine the redshift variation of the limiting mass within each BIMA field, we make mock, on-axis ($\theta = 0$) observations of these 48 clusters at different redshifts. The mass limit at redshift z is determined using simulated clusters output at that same redshift.

For each of these mock observations, we convert the Compton y map determined from the hydrodynamic simu-

TABLE 1
BASIC DESCRIPTION OF THE FIELDS [†]

Field *	Pointing Center (J2000)		Beam Size ("×")	Time (hr)	rms (μK)	rms ($\mu\text{Jy bm}^{-1}$)
	α	δ				
p1643	16 45 11.3	+46 24 56	98.3×116.1	43.1	25.1	191
VLA1312	13 12 17.4	+42 38 05	95.2×113.4	35.5	31.0	223
pss0030	00 30 16.4	+17 02 40	99.1×115.5	36.6	26.6	203
BF0028	00 28 04.4	+28 23 06	108.9×118.8	77.6	11.5	99
HDF_BIMA	12 36 49.4	+62 12 58	110.9×122.0	32.0	18.6	168
BF1821	18 21 00.0	+59 15 00	108.4×122.4	43.5	22.4	224
BF0658	06 58 45.0	+55 17 00	105.2×148.0	44.7	29.3	304

[†]From Holzapfel et al. (2000a)

*Field names are referred in Holzapfel et al. (2000a) as BDF1–7, respectively

lations to visibilities using a Fast Fourier Transform (FFT) according to the prescription outlined in §2.1. Visibilities are then sampled from this map at the same locations in u - v space probed by the BIMA observations in each field. We add Gaussian noise to the visibility that is appropriate given the uncertainty of that same visibility in the BIMA observations; in fact, we scale these uncertainties down by a factor, which corresponds to a longer observation with BIMA (using $\sigma_V \propto 1/\sqrt{t_{obs}}$). This reduction in noise allows a more accurate estimate of the cluster mass corresponding to a particular detection significance (see Fig 1), and this scaling can be removed after the detection. We have tested the accuracy with which one can introduce these longer observing times and then remove them after the mock detection by calculating the limiting mass for a wide range of observing time scale factors. Results indicate that the limiting mass corresponding to a 2σ detection is independent of the exact scale factor used (assuming it is large) at the 1% level.

2.3.1. The Hydrodynamical Simulations

The cluster models used in the mock observations are from an ensemble of 48 hydrodynamical cluster simulations in four Cold Dark Matter (CDM) cosmologies: (1) Standard CDM (SCDM: $\Omega_M = 1$, $\sigma_8 = 0.6$, $h = 0.5$, $\Gamma = 0.5$), (2) Tilted CDM (τ CDM: $\Omega_M = 1$, $\sigma_8 = 0.6$, $h = 0.5$, $\Gamma = 0.24$), (3) Open CDM (OCDM: $\Omega_M = 0.3$, $\sigma_8 = 1$, $h = 0.8$, $\Gamma = 0.24$), and (4) Lambda CDM (Λ CDM: $\Omega_M = 0.3$, $\Omega_\Lambda = 0.7$, $\sigma_8 = 1$, $h = 0.8$, $\Gamma = 0.24$). Here h is the Hubble parameter in units of 100 km/s/Mpc. The initial conditions of the simulations are Gaussian random fields consistent with a CDM transfer function with index Γ (Davis et al. 1985).

The simulation scheme is particle-particle-particle-mesh smoothed-particle hydrodynamics (Evrard 1988, P3MSPH), with fixed intracluster gas mass fraction $f_{ICM} = 0.2$ (but we correct to $f_{ICM} = 0.12$, consistent with observations for $h = 0.70$; Mohr et al. 1999). Radiative cooling and heat conducting are ignored. The 48 simulated clusters have similar fractional mass resolution; the spatial resolution varies from 125–250 kpc. The masses of the final cluster sample vary by an order of magnitude. More detail on the simulations can be found in other analyses that have employed these same simulations (Mohr & Evrard 1997; Mohr et al. 1999; Mathiesen et al. 1999; Mathiesen & Evrard 2001).

Following procedures described in Evrard (1990), we

create Compton y parameter images along three orthogonal lines of sight for each cluster. For these calculations each cluster is imaged as though it were at a redshift $z = 0.06$. These projections serve as templates for the mock observations used to determine the limiting masses. In determining the limiting mass at a redshift z , we use the simulation outputs that correspond to that redshift; this ensures that our mass limit includes the effects of cluster structural evolution with redshift.

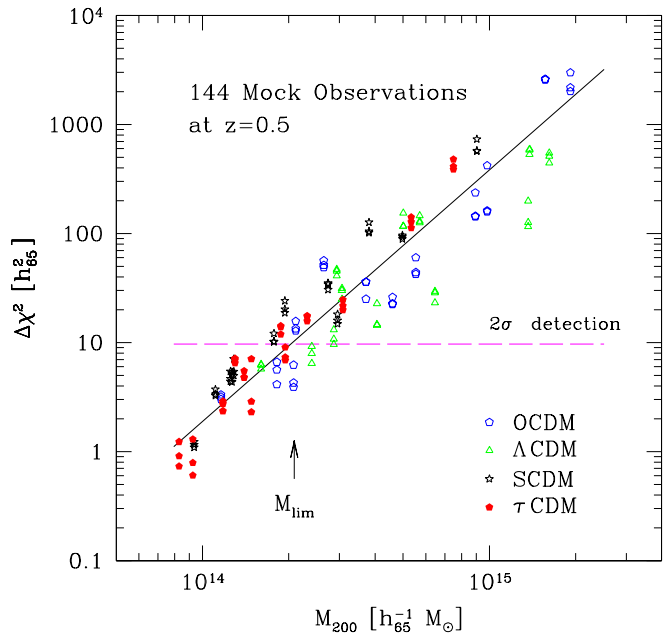


FIG. 1.— The detection significance, measured as $\Delta\chi^2$, of mock observations of the 48 simulated clusters in one BIMA field (BF0028). Each cluster is observed along three orthogonal lines of sight. The intersection of the best-fit line with the $\Delta\chi^2 = 9.7$ line (corresponding to 2σ detection) determines the detection threshold mass M_{lim} . Here and afterwards $h_{65} \equiv h/0.65$.

2.3.2. Mock Cluster Detection

We analyze the mock observations using software developed to analyze real cluster observations (Reese et al. 2000). For simplicity and fast computation, we model the ICM density distribution using a spherical β model (Cavaliere & Fusco-Femiano 1978) with $\beta = 4/3$. For this value of β , the Fourier conjugate of the model is an exponential (see Eqn 6); additionally, this value is roughly consistent with the best fits to the SZE decrement images from the

simulations ($\langle \beta \rangle = 1.1$). Furthermore, we do not include the effects of the primary beam, and this allows us to bypass the FFT normally required in each fit iteration. This fast detection scheme should be appropriate near the detection threshold, where there is little information about the detailed shape of the cluster.

For each cluster we fit the core radius and the central decrement simultaneously by minimizing the χ^2 difference between the fit and the observations. We do not actually simulate “finding” the clusters within the field; rather, we assume that the approximate location of each cluster can be obtained by examining the BIMA observation in the image plane. We are currently exploring other techniques, which would allow detection and characterization of clusters in the Fourier domain. The χ^2 difference between the null model and the best fit model ($\Delta\chi^2 \equiv \chi_{null}^2 - \chi_{fit}^2$) serves as a measure of the detection significance. At a point on the field (θ, ϕ) and a redshift z , we repeat this procedure for all 48 cluster models (viewed along three axes) and obtain a tight correlation between cluster mass M_{200} and detection significance $\Delta\chi^2$. We determine the best-fit of the $\Delta\chi^2 - M_{200}$ relation by a downhill simplex method (Press et al. 1992). For 2 degrees of freedom the 95% confidence limit corresponds to $\Delta\chi^2 = 9.7$. The limiting mass $M_{lim}(\theta, \phi, z)$ is the intersection of the best-fit line with the $\Delta\chi^2 = 9.7$ line, and the detection efficiency function $f(M)$ is constructed from the scatter about the best-fit line. Fig 1 is a plot of $\Delta\chi^2$ versus M_{200} for mock observations on field BF0028, observed on-axis ($\theta = \phi = 0$) at $z = 0.5$.

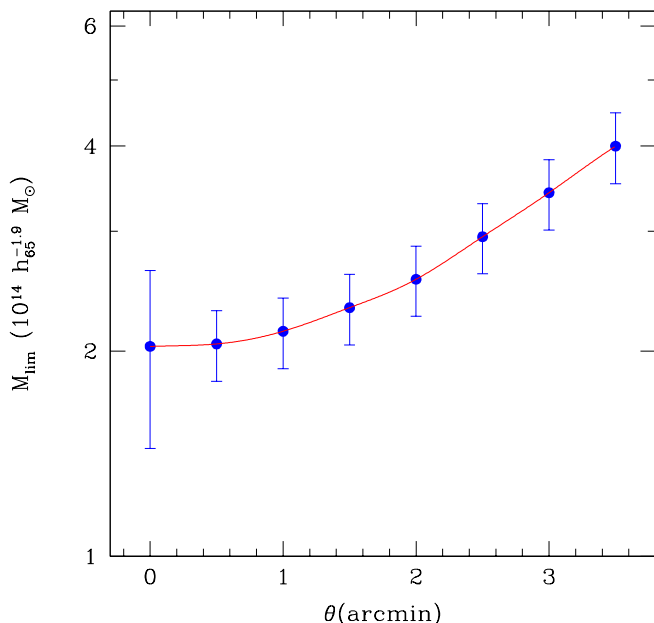


FIG. 2.— The angular dependence of the limiting mass in the field BF0028. These limiting masses are determined using mock observations of simulated galaxy clusters. The mock observations mimic the actual observations of each BIMA field. Also shown is the spline, which we use to determine M_{lim} for arbitrary off-axis angle. (For the h dependence of M_{lim} see the Appendix.)

We have compared the limiting mass given by the faster detection algorithm described above (fixed $\beta = 4/3$ model and no primary beam) with that obtained from full β -model fitting that includes the effects of the primary beam.

The differences in the derived limiting mass M_{lim} are at the 1% level.

The rms scatter with respect to the $\Delta\chi^2 - M$ correlation gives the uncertainty in the limiting mass and determines $f(M)$. We model the detection efficiency by assuming Gaussian scatter in the $\log \Delta\chi^2 - \log M$ relation. Taking $\lambda = \log \Delta\chi^2$ and the rms scatter in λ to be σ_λ , we can write the detection efficiency as

$$f(M) = \frac{1}{\sqrt{2\pi\sigma_\lambda^2}} \int_{\lambda_{min}}^{\infty} d\lambda e^{-\frac{1}{2}\left(\frac{\lambda - \overline{\lambda(M)}}{\sigma_\lambda}\right)^2} \quad (7)$$

where $\lambda_{min} = \log 9.7$ (i.e. a 2σ detection) and $\overline{\lambda(M)}$ is the best fit $\log \Delta\chi^2$ for mass M .

Applying the same procedure for each deep field, we obtain $M_{lim}(\theta, \phi, z)$ and $f(M)$ at specific values of (θ, ϕ, z) for all fields. Values of M_{lim} for arbitrary (θ, ϕ, z) require an interpolation scheme. We take the limiting mass to be $M_{lim}(\theta, \phi, z) = M_{lim}(\theta, \phi, z = 0.5) \times r(z)$, where $M_{lim}(\theta, \phi, z = 0.5)$ encodes the angular dependence of the limiting mass at redshift $z = 0.5$, and $r(z)$ is the redshift behavior of the mass limit at $\theta = \phi = 0$, normalized so that $r(z = 0.5) = 1.0$.

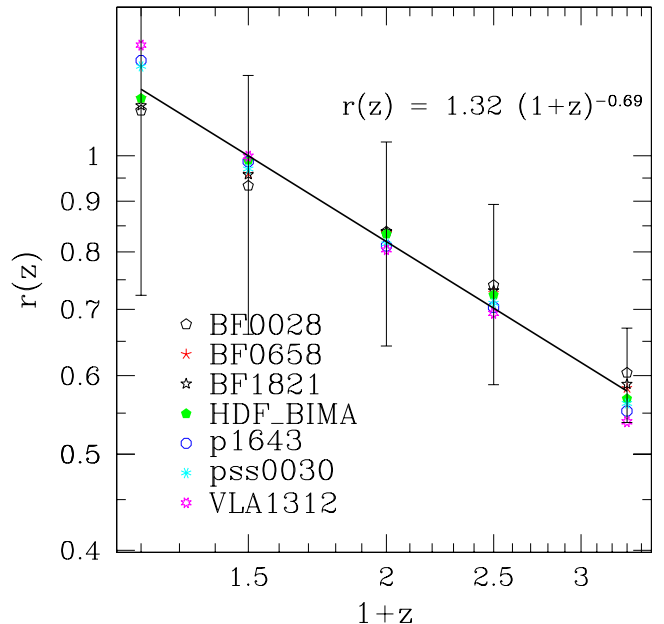


FIG. 3.— The redshift dependence of the limiting mass. Points for each BIMA field denote the measured limiting masses at 5 redshifts relative to the value at $z = 0.5$. The best fit power law $r(z)$ to the ensemble is noted in the figure. Error bars are shown only for field BF0028.

To determine the angular variation of the limiting mass, we average the values of $M_{lim}(\theta, \phi, z = 0.5)$ over the azimuthal angles ϕ that are evenly spaced in the 360° circle; we sample off-axis angles θ at $\theta = 0'5, 1'0, 1'5, 2'0, 2'5, 3'0$ and $3'5$, where the maximum θ is close to the HWHM of the beam. The limiting masses at arbitrary off-axis angles are calculated using a spline. Fig 2 contains a plot of the angular dependence of M_{lim} in BF0028.

We determine the redshift dependence $r(z)$ using the limiting mass measurements at redshifts $z = 0.2, 0.5, 1.0, 1.5$ and 2.3 . Fig 3 contains a plot of the on-axis limiting mass M_{lim} for each field at these five different redshifts. A single power-law provides an adequate

description of the redshift behavior of the limiting mass in all seven fields. The scatter of the limiting masses around this best fit power-law is comparable to or smaller than the estimated uncertainties in these limiting masses.

We have also examined the angular variation of the scatter σ_λ for all off-axis positions sampled (at $z = 0.5$). The variation is small (e.g. the *rms* variation of σ_λ in the field BF0028 is 6.6%). There is also some redshift variation of σ_λ for each field (at $\theta = \phi = 0$). With a large sample of simulated clusters it will be possible to better determine the scatter in detectability σ_λ , but for this analysis we adopt a single σ_λ for each field. We use this in determining $f(M)$ at all off-axis angles θ and redshifts z .

Finally, as previously noted, the cosmology dependence in M_{lim} is from the angular diameter distance to the clusters. Because we probe a wide range of cosmological models, while our limiting mass is derived from a fiducial cosmology with $(\Omega_M, \Omega_\Lambda) = (0.3, 0.0)$, we rescale M_{lim} to be consistent with the model considered. Following Haiman et al. (2001), the limiting mass in a given cosmology at redshift z is $M_{lim}(z)h = M_{lim}^*(z)h^*(\tilde{d}_A(z)/\tilde{d}_A^*(z))^{1.2}$, where quantities with an asterisk denote that in the fiducial cosmology, and $\tilde{d}_A(z) \equiv h d_A(z)$ is the Hubble-parameter-independent part of the angular diameter distance. We discuss the Hubble parameter dependence of the survey in the Appendix.

3. EXPECTED YIELDS FOR ANY COSMOLOGY

From the discussions in §2 it is clear that in calculating the expected number of clusters (Eqn 1), M_{lim} , $f(M)$ and the functional form of the mass function are important ingredients. For the mass function we adopt the fitting formula given by Jenkins et al. (2001), obtained from large-scale N-body simulations of structure formation:

$$\frac{dn}{dM}(M, z) = -0.315 \frac{\rho_0}{M} \sigma^{-1} \frac{d\sigma}{dM} e^{-|0.61 - \ln \sigma|^{3.8}} \quad (8)$$

where ρ_0 is the present-day matter density and $\sigma(M, z)$ is *rms* variation in overdensity on mass scale M and at redshift z . This fitting formula provides a more accurate abundance of collapsed halos than does the classical Press-Schechter mass function (Press & Schechter 1974). In both Jenkins and Press-Schechter mass functions, the form and amplitude of $\sigma(M)$ is one essential component.

We calculate $\sigma(M)$ by directly integrating the power spectrum of density fluctuations, masked by the Fourier conjugate of a spherical top-hat window function $W(k, R)$ over wavenumber k , where R denotes the radius of the spherical top-hat. We assume the initial power spectrum is of the form $P_{ini}(k) \propto k^n$, which can be related to the power spectrum $P(k, z)$ at any redshift after the epoch of matter-radiation equality by the CDM transfer function $T(k)$ and the growth function $D(z)$. We use the transfer function given by Eisenstein & Hu (1998), and the baryon density parameter $\Omega_B = 0.019 h^{-2}$ which derives from deuterium abundance measurements (Burles & Tytler 1998). We write $P(k, z) \propto k^n T^2(k) D^2(z)/D^2(0)$, where $D(z) = g(\Omega(z))/1+z$ and $g(\Omega(z))$ is the growth-suppression factor given by Carroll et al. (1992).

We employ a variety of strategies for normalizing $\sigma(M)$. These include (1) matching the amplitude of the power spectrum on the largest scales to the constraints from cosmic microwave background anisotropy measurements (e.g.

Bunn & White 1997; Majumdar & Subrahmanyan 2000), (2) reproducing the local cluster abundance (e.g., Viana & Liddle 1999), and (3) simply adopting the normalization as a free parameter to be constrained using the BIMA deep field observations. The first approach probes the power spectrum on much larger scales than the last two.

Using the Jenkins et al. (2001) expression for the mass function dn/dM requires adopting their halo mass definition. They use M_{SO180} masses, corresponding to the mass enclosed within the region that has a mean overdensity of 180 times the *background* density. The limiting masses we estimate using mock observations of hydrodynamic simulations are all M_{200} 's—that is, masses enclosed in regions with mean overdensity of 200 with respect to the *critical* density. We convert from M_{200} to M_{SO180} using the “universal” halo density profile with a concentration parameter $c = 5$ (Navarro et al. 1997). Any differences between real cluster halos and our adopted model will manifest themselves as a systematic error in the mass selection function $f(M)$. We account for these systematics in our analysis (see §4.3).

With these ingredients, we calculate the expected number of detected clusters $\langle N \rangle$ in our BIMA fields. Rewriting Eqn 1 to reflect our approach, the expected number of clusters detected in a given field is:

$$\langle N \rangle = \int_0^{\theta_{max}} d^2\theta \int_0^{z_{max}} dz d_A^2 \frac{c(1+z)^2}{H(z)} \int_0^\infty dM f \frac{dn}{dM}, \quad (9)$$

where $\theta_{max} = 3'5$, $f = f(M, \theta, z)$ is the detection efficiency and dn/dM is the cluster abundance given in Eqn 8. We truncate the redshift integration at some maximum redshift z_{max} , beyond which the cluster formation and evolution is uncertain. For $\Omega_M = 1.0$ models, z_{max} is set to be 4, and for all other models considered $z_{max} = 10$.

4. RESULTS

We use the techniques described above to constrain cosmological parameters with the BIMA deep survey fields. We restrict our analysis to two sets of models: (1) those with purely dark matter ($\Omega_M \leq 1$ & $\Omega_\Lambda = 0$, *open* models hereafter) and (2) those with dark matter and a cosmological constant ($\Omega_\Lambda \geq 0$ and $w = -1$, where $w \equiv p/\rho$ characterizes the equation of state) that are geometrically flat ($\Omega_M + \Omega_\Lambda = 1$, *flat* models hereafter).

Let us denote any cosmological model to be considered as $\{\Omega, \sigma_8\}_j$. To determine the probability of consistency of this model with our data, we calculate the expected number of detected clusters $\langle N \rangle_i$ for each BIMA field i . Suppose the detection of clusters is a Poisson random process, the probability of observing zero clusters in field i is then $P_i(\{\Omega, \sigma_8\}_j) = e^{-\langle N \rangle_i}$. The total probability of observing zero clusters in each of the seven fields is then $P_{tot}(\{\Omega, \sigma_8\}_j) = \prod_i P_i$.

Below we explore the cosmological information contained in the BIMA fields themselves (§4.1), and then we examine constraints from the BIMA fields together with the local, massive cluster abundance (§4.2) and together with the CMB constraints on the power spectrum normalization (§4.3). We end this subsection with a discussion of our approach to including the uncertainties in the survey limiting mass, the Hubble parameter, the COBE normalization parameters, and the effects of sample variance.

4.1. Using Only BIMA Deep Fields

Fig 4 contains the cosmological constraints on parameters σ_8 and Ω_M from the BIMA survey fields alone. Solid lines show the equivalent 1σ and 3σ Gaussian probabilities for flat models, and dashed lines show similar confidence regions for the open models. We have explored parameter ranges $0.1 \leq \Omega_M \leq 1.0$ and $0.3 \leq \sigma_8 \leq 2.0$. These constraints are upper limits, because for fixed Ω_M it is possible to reduce the number of clusters by lowering σ_8 . As expected, high σ_8 can be ruled out. We fit the 2σ contours to give a rough constraint on σ_8 (for $0.1 \leq \Omega_M \leq 1.0$): $\sigma_8 < 1.00 \Omega_M^{-0.43\Omega_M-0.22}$ (flat) and $\sigma_8 < 1.01 \Omega_M^{-0.40\Omega_M-0.14}$ (open) at 95% confidence level. In calculating these results, the uncertainties in detection efficiency are included (see §4.3 for a detailed discussion).

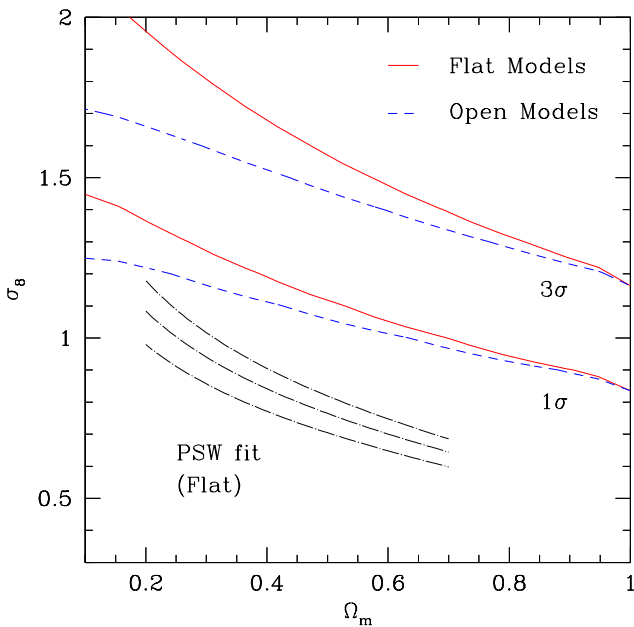


FIG. 4.— Constraints on Ω_M and σ_8 for both flat (solid line) and open (dashed line) universe models. The range of Ω_M considered is $0.1 \leq \Omega_M \leq 1.0$, and the range of σ_8 is $0.3 \leq \sigma_8 \leq 2.0$. Results from the Pierpaoli et al. (2001) analysis of the temperature function are shown (dot-dashed line) with $\pm 1\sigma$ range.

For comparison, dot-dashed lines in Fig 4 indicate the preferred values and 1σ confidence regions derived from the local temperature function of 38 massive clusters (Pierpaoli et al. 2001, hereafter PSW). The PSW constraints are only for flat cosmologies. These constraints are clearly much stronger than those from the BIMA survey. A larger solid angle and higher sensitivity SZE survey which delivers SZE cluster detections, is required to move from upper limits to a preferred range of values, as in the PSW analysis. These two surveys – a large solid angle local survey and a small solid angle high redshift survey – are complementary (rather than redundant); in §4.2 we explore joint constraints of the deep BIMA survey and a similar but simpler approach to the local abundance analysis.

We can understand the shape of the confidence region as follows. For fixed Ω_M , models of higher σ_8 lead to larger $\langle N \rangle$, which are more inconsistent with the BIMA survey. The behavior of the probability along lines of fixed σ_8 is explained with the help of Fig 5. In the figure we con-

sider three flat models and one open model with $\sigma_8 = 1$: flat $\Omega_M = 0.1$ (solid/red), flat $\Omega_M = 0.5$ (dashed/blue), flat $\Omega_M = 1$ (dotted/black) and open $\Omega_M = 0.5$ (dot-dashed/green). From top to bottom the panels contain the cluster redshift distribution $dN/dz d\Omega$, the comoving differential volume element $dV/dz d\Omega = c d_A^2 (1+z)^2 / H(z)$, the detectable cluster number density or abundance $n = \int_0^\infty dM dn/dM f(M)$, and the limiting detectable mass M_{lim} . In the case of the limiting mass, we show the ratio of M_{lim} in each model to its value in the $\Omega_M = 1$ model. The curves in the top panel are essentially the products of those in the second and third panels. The behavior of the volume element reflects that of the angular diameter distance, which changes only slowly beyond $z \sim 1$. At $z > 1$, the BIMA survey is probing an order of magnitude higher volume in the $\Omega_M = 0.1$ model than in the $\Omega_M = 1$ model.

The behavior of the abundance evolution in each model is primarily a reflection of the way $\sigma(M, z=0)$ is normalized: although σ_8 is set to be unity for all three models, the mass contained in $8h^{-1}$ Mpc scale ($\equiv M_{cl}$) differs for each model because $M_{cl} \propto \Omega_M$. The result is that, at low mass range $M \gtrsim M_{lim}$, $\sigma(M, z)$ of high Ω_M models is always larger. Interestingly, for masses near the detection limit the reduction in the amplitude of $\sigma(M)$ for the low Ω_M models at fixed σ_8 more than compensates for the more rapid evolution of density perturbations in the high Ω_M models. Furthermore, the steepness of the mass function implies that contributions to the number density come mostly from the systems with masses near the detection limit. Finally, the limiting masses for low density models are larger than that of high density models. Together, these effects lead to lower number densities of detectable clusters in the low Ω_M models.

Finally, consider why the BIMA survey constrains open models more strongly than flat models. As also shown in Fig 5, the dot-dashed/green line represents an $\Omega_M = 0.5$ open model. We see there is little difference in the volume element between two $\Omega_M = 0.5$ models, while the difference in abundance at high redshifts is large. This can be understood from the slower growth of structure in open models; in short, open models at fixed σ_8 produce more high redshift clusters than flat models and are thus more inconsistent with the data.

4.2. BIMA Deep Fields Plus Local Abundance

In this case, we use both the BIMA deep fields and a measurement of the local massive cluster abundance. Calculating the constraints for each Ω_M requires two steps: (1) determining the σ_8 , which reproduces the local abundance of massive clusters above some fiducial temperature kT_X , and (2) then estimating the expected number of clusters $\langle N \rangle_i$ for each BIMA field i . We determine σ_8 by requiring that $n(M > M_{th})$ matches the observed local cluster abundance, where M_{th} is the mass corresponding to the X-ray temperature cutoff of the sample. We adopt the value given by Viana & Liddle (1999), which is for clusters of X-ray temperature greater than 6.2 keV at $z = 0.05$ (see also Henry 1997). The values of σ_8 we obtain do not differ much from those of Pierpaoli et al. (2001), within the range of $0.2 \leq \Omega_M \leq 0.7$. We then calculate $\langle N \rangle_i$ in each BIMA field and the corresponding probability for that cosmological model.

However, combining these two datasets provides very weak, if any, constraints on the density parameter; essentially all models considered are consistent with the data. Models with lower matter density are relatively more incompatible, but even at the model with lowest density ($\Omega_M = \Omega_B$), the exclusion probability is still weaker than 1σ .

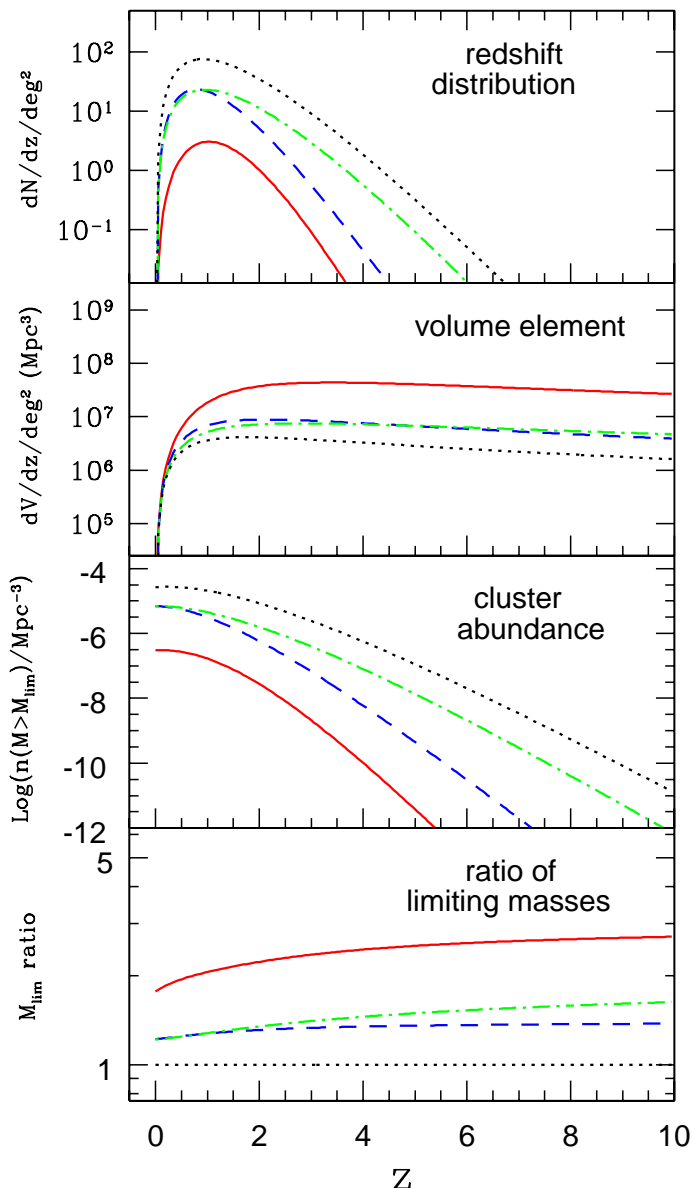


FIG. 5.— The behavior of the confidence regions in Fig 4 results from several competing effects. From top to bottom, we show the cluster redshift distribution, the volume element, the cluster abundance, and the limiting mass for three flat models at fixed $\sigma_8 = 1$ and $h = 0.65$: $\Omega_M = 0.1$ (solid), $\Omega_M = 0.5$ (dashed), and $\Omega_M = 1$ (dotted). Also shown is an $\Omega_M = 0.5$ open model (dot-dashed). The limiting mass panel contains the ratio of M_{lim} to that in the $\Omega_M = 1$ model.

This method produces a *lower* limit on Ω_M because we are requiring the local cluster abundance to be the same in all cosmological models; in this scenario, those models with slower growth of density perturbations (i.e. low Ω_M models) produce more high redshift clusters and are therefore more inconsistent with our SZE survey.

4.3. BIMA Deep Fields Plus COBE

By combining the BIMA deep fields with a COBE normalization for the power spectrum of density fluctuations, it is possible to place an upper limit on Ω_M . The COBE measurements on large angular scale anisotropy can be used to constrain the amplitude of the power spectrum on the scale of the present epoch horizon ($3000 \sim 4000 h^{-1}$ Mpc). Taking the amplitude of modes on this scale to be δ_H , we can write the power spectrum in the form $P(k, z) = 2\pi^2 \delta_H^2 (c/H_0)^{3+n} k^n T^2(k) D^2(z)/D^2(0)$ (e.g. Bunn & White 1997; Eisenstein & Hu 1998). We adopt the fitting function for parametrization of δ_H provided by Bunn & White (1997), assuming no contributions from primordial gravitational waves. For the index of primordial power spectrum, we adopt the BOOMERANG measurement $n = 0.96^{+0.10}_{-0.09}$ (Netterfield et al. 2001). Although we adopt different values of Ω_B and H_0 than those used by Bunn & White (1997), we do not rescale $\delta_H(\Omega_M, n)$ to account for these differences; the change in amplitude of δ_H from this rescaling would be small compared to the statistical uncertainty on δ_H itself. Normalizing the power spectrum in this way leads to σ_8 that increases with Ω_M .

Because σ_8 increases with Ω_M , we expect the COBE normalized SZE survey constraints to provide an upper limit on Ω_M . From Fig 6, we find that the 95% confidence upper limit on Ω_M in flat (open) models is $\Omega_M < 0.63$ ($\Omega_M < 0.73$). These upper limits include uncertainties in the SZE flux–virial mass relation, the Hubble parameter, the COBE normalization and the power spectrum index, as well as the effect of the sample variance. Below we provide further detail.

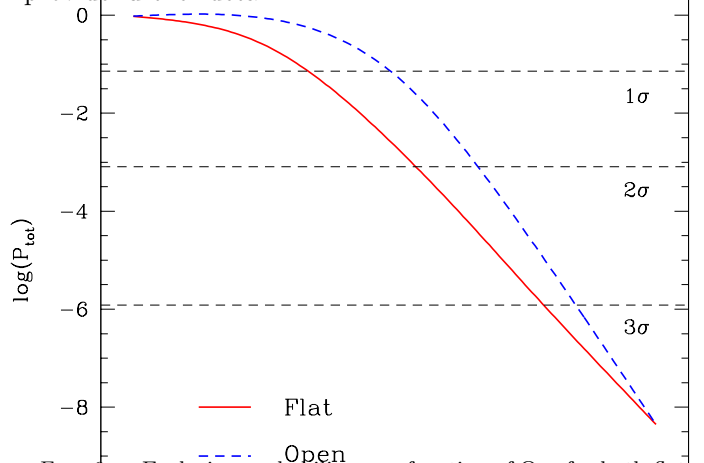


FIG. 6.— Exclusion probability as a function of Ω_M for both flat and open models, when the power spectrum is normalized to COBE. Uncertainties in virial mass, H_0 , δ_H , and n as well as the sample variance are included (see §4.3). In flat (open) models, $\Omega_M < 0.63$ (0.73) at 95% confidence.

4.3.1. Detection Efficiency

The key to interpreting cluster surveys is connecting the observables (cluster SZE visibility in this case) to the halo virial mass. This generally involves a mass–observable scaling relation, which we term the visibility–mass relation – and a model for the redshift evolution of this relation. As has already been discussed, we use hydrodynamical simulations to define this visibility–mass relation, and we parametrize the redshift evolution of this visibility–mass relation by making mock observations of clusters output at a range of redshifts. The visibility–mass relation for an

interferometric SZE survey is similar to the better known mass–temperature relation in an X-ray cluster survey. In the X-ray survey the cluster temperature is used as the mass predictor.

We model these uncertainties by introducing a 40% systematic uncertainty in the normalization of the $\Delta\chi^2$ –mass relation (see Fig 1), corresponding to a 20% uncertainty in the visibility–mass relation. From Eqn 5 it is clear that this corresponds to a systematic uncertainty in the limiting cluster mass (remember $f(M_{lim}) \equiv 0.5$) of $\sim 16\%$ (see the discussion in §). We model this systematic uncertainty as a Gaussian distribution, and marginalize over this systematic by integrating the probability obtained from Eqn 9 over the Gaussian distribution in M_{lim} .

4.3.2. Hubble Parameter H_0 and Power Spectrum Parameters δ_H and n

Our constraints on Ω_M are sensitive to the Hubble parameter through its effect on the volume element, the amplitude of $\sigma(M)$, the critical density and the mass limit. Rather than choosing a particular value of H_0 , we assume a Gaussian distribution in H_0 centered on a fiducial value of 65 km/s/Mpc with a 1σ uncertainty of 10%. We also account for uncertainties in the COBE normalization amplitude δ_H and the primordial power spectrum index n . We take both the distributions of δ_H and n to be Gaussian, with dispersions of 7% (Bunn & White 1997) and 10% (Netterfield et al. 2001), respectively. The final probability of consistency with the SZE survey is calculated by integrating over these Gaussian distributions.

4.3.3. Sample Variance

To assess the importance of sample variance on our Ω_M constraints, we follow the approach of Hu & Kravstov (2002). Because our survey fields are small, we approximate each field as a series of circular pillboxes, each of radius $3'5$ and thickness $\Delta z = 0.16$, arranged in increasing redshift. We calculate the covariance matrix σ_{ij}^2 between redshift bins i and j

$$\sigma_{ij}^2 = n_i \bar{b}_i n_j \bar{b}_j D_i D_j \int \frac{d^3k}{(2\pi)^3} W_i W_j^* P(k), \quad (10)$$

where n is the number of detected clusters in the bin, \bar{b} is the mass function weighted mean bias, D is the growth function and W is the Fourier transform of the pillbox window function at each redshift. We estimate the sample variance σ_s^2 by summing the matrix elements. We have only included the terms with $|i - j| \leq 1$, because other elements are negligible, as noted by Hu & Kravstov (2002). The exclusion probability for a given cosmology is then

$$P(\Omega_M) \propto \int_0^\infty d\mu e^{-\frac{(\mu - \langle N \rangle)^2}{2\sigma_s^2}} e^{-\mu} \quad (11)$$

up to a suitable normalization factor. It turns out, the inclusion of the sample variance only weakens our constraints to a small extent, corresponding roughly to a 1% upward shift in the constraint curve in Fig 6.

4.3.4. Field Selection and Non-detection Significance

These fields were not chosen randomly, and the selection criteria could potentially bias the expected number of detected clusters. Fields p1643 and VLA1312 are centered in

directions claimed to have cluster SZE decrements (Jones et al. 1997; Richards et al. 1997) that have not been confirmed by higher sensitivity observation (Holzapfel et al. 2000b). The field pss0030 is in the direction of a radio-quiet quasar. The other 4 fields were chosen to be evenly distributed in right ascension, at convenient declinations, in regions of low dust-emission and free of bright point sources at 1.4 GHz, in optical and in X-ray. As pointed out by Dawson et al. (2001), radio point sources may trace large scale structure, preferentially populating clusters. If so, as a whole the fields may be biased to contain fewer than the expected number of clusters.

Clearly, our constraints on Ω_M are valid only if these fields provide an unbiased sample of the universe. One could also ask whether it is surprising that no clusters were detected in the deepest and largest SZE survey to date. If the fields are unbiased, then the answer is no, if we live in a low matter density universe. If the fields are biased against finding clusters, then this would make it even less surprising that no clusters were detected.

Our results also depend to some degree on our interpretation of the Holzapfel et al. (2000a) search for cluster SZE decrements. Specifically, we present results assuming that no clusters were detected at or above the 95% confidence level, whereas the authors provide no quantitative discussion. Clearly, the authors were very interested in finding galaxy clusters, and no firm detections were made (Holzapfel et al. 2000a,b). A reanalysis of the data searching for clusters in much the same way that we have searched for clusters in our mock observations would be ideal, and such an analysis is ongoing (Carlstrom, private communication). Here we simply report the constraints on Ω_M if cluster detections in the BIMA deep fields can only be ruled out at the 3σ and 4σ level. In these cases, clusters would have to be more massive to produce these stronger detections, and therefore one would generally expect fewer detections for a given density parameter. Thus, the 95% confidence upper limit would weaken to $\Omega_M < 0.70$ and $\Omega_M < 0.77$, respectively. In general, our results are relatively insensitive to the exact characterization of the non-detection significance.

5. SUMMARY AND DISCUSSION

We describe a systematic analysis of an interferometric SZE survey carried out at BIMA with the Carlstrom–Joy 30 GHz receivers. The data were taken from observations of the CMB anisotropy on arcminute scale ($l \sim 5500$), in which no anisotropy and no galaxy clusters were detected (Holzapfel et al. 2000a,b). We use these data to study the allowed range of cosmological parameters σ_8 and Ω_M . In our analysis, we consider models that are flat with a cosmological constant ($\Omega_M + \Omega_\Lambda = 1$) and models that are open with no cosmological constant.

Our analysis hinges on our ability to calibrate the survey sensitivity or galaxy cluster selection function. To this end, we use mock interferometric observations of hydrodynamical cluster simulations to determine the selection function for each of the seven fields and as a function of redshift and position within that field. Relying on hydrodynamical simulations to calibrate the survey sensitivity introduces significant uncertainties, which can be reduced once empirical calibration using large surveys that include

detailed followup observations are available. For this analysis we estimate the scale of the uncertainties that come with using hydrodynamical cluster simulations and include those uncertainties in determining our constraints on the cosmological parameter Ω_M .

With BIMA survey data alone, we obtain a 95% confidence upper limit on $\sigma_8(\Omega_M)$: $\sigma_8 < 1.00 \Omega_M^{-0.43\Omega_M-0.22}$ for flat, and $\sigma_8 < 1.01 \Omega_M^{-0.40\Omega_M-0.14}$ for open models. Combining the BIMA survey with external constraints on the power spectrum allows us to constrain Ω_M alone. In combination with the local abundance of high temperature X-ray clusters, the BIMA data lead only to a trivially weak lower limit: $\Omega_M > \Omega_B$. In combination with the COBE normalization of the power spectrum, the data provide an upper limit on Ω_M : $\Omega_M < 0.63$ for flat models, and $\Omega_M < 0.73$ for open models at 95% confidence. Included in the constraints on Ω_M are 40% uncertainties in the cluster visibility–mass relation as well as published uncertainties on the Hubble parameter and power spectrum normalization δ_H and spectral index n . We also include the effects of sample variance.

These constraints are valid only if these BIMA fields represent an unbiased sample of the universe. The field selection in this survey is somewhat suspect, with four of the seven fields specifically chosen to exclude bright radio, X-ray and optical point sources. A firm interpretation of our results is that – if the fields are an unbiased clusters survey – we have shown that within the context of the cosmological models favored today, we expect no clusters to have been detected. If the survey was biased against finding clusters, then our constraints on Ω_M weaken, and it is even less surprising that no clusters were detected. Of course, if the survey were biased toward finding clusters, then finding none would imply tighter constraints on Ω_M . We eagerly await planned SZE surveys of larger and perhaps better chosen fractions of the universe.

In previous work, Majumdar & Subrahmanyam (2000) studied constraints on Ω_M by comparing simulated SZE maps with the upper limit on the arcminute–scale anisotropy in CMB obtained by Subrahmanyam et al. (2000) using the Australia Telescope Compact Array (ATCA) at 8.7 GHz. Their 95% confidence upper limit is $\Omega_M < 0.8$ for open models. This result is clearly consistent with ours, but there are important differences in the analysis and the data. First, the ATCA survey has lower sensitivity than the BIMA survey, yielding a 95% confidence limit of $Q_{flat} < 25 \mu\text{K}$ compared to the BIMA survey constraints of $Q_{flat} < 14.1 \mu\text{K}$. Second, their focus was on reproducing the statistical properties of the noise in the sky maps, whereas we have on the non–detection of clusters. Third, our modeling technique is more sophisticated than theirs through its use of hydrodynamical cluster simulations that incorporate the effects of cluster morphology and internal structure and the evolution of these properties with redshift. And fourth, we model the redshift evolution of the cluster abundance using the results from the latest N–body studies of structure formation (Jenkins et al. 2001), whereas they modeled cluster abundance

using the original Press–Schechter formalism. We believe that the techniques we outline in this manuscript provide a viable approach for analyzing the forthcoming interferometric SZE surveys that will use much higher sensitivity instruments to survey larger portions of the sky.

In short, the principle improvement of our analysis over previously existing analyses and estimates of survey yields include (1) the direct accounting for the uncertainty in the cluster detectability (specifically, we model the scatter in the detection significance–virial mass relation and we include the uncertainty in the normalization of the SZE visibility–virial mass relation), (2) the modeling of the survey sensitivity as a function of position on the sky, (3) the inclusion of uncertainties on other cosmological parameters of interest, and (4) an accounting for the effects of sample variance on our Ω_M constraint.

In addition, we have examined the h dependence of the survey limiting mass (see Appendix), showing that for this interferometric survey, which includes sensitivity to cluster shape *and* flux, the h dependence departs from the flux limited survey expectation $M_{lim} \propto h^{-8/5}$ to a steeper dependence of $M_{lim} \propto h^{-11/6}$. Similar departures would be expected for other interferometric surveys.

Large solid angle, high redshift SZE cluster surveys can in principle provide a wealth of information on structure evolution and cosmology. Because of its redshift–independent nature, the SZE is a powerful tool in studies of the high redshift universe. An interferometric SZE survey has advantages such as superb angular resolution and the ability to separate point source contamination from the extended clusters (Holder et al. 2000; Kneissl et al. 2001). Future SZE surveys will have much higher sensitivity than the BIMA survey analyzed here, and will be carried out with the Sunyaev–Zel’dovich effect Array (SZA, Holder et al. 2001), the Arcminute Microkelvin Imager (AMI, Kneissl et al. 2001), and the Arcminute Mm-wave interferometer for Background Anisotropy (AMiBA, Lo et al. 2000). These surveys are expected to detect hundreds of clusters, and these large, high redshift cluster samples will be invaluable to cosmological studies, enabling tests of the mix of dark energy and dark matter in our universe and measurements of the nature of this dark energy (e.g. Barbosa et al. 1996; Haiman et al. 2001; Holder et al. 2001; Fan & Chiueh 2001; Mohr 2001; Weller et al. 2001; Hu & Kravstov 2002).

We acknowledge many illuminating conversations with Subha Majumdar. We thank Bill Holzapfel and John Carlstrom for providing details about the BIMA deep field observations, and we thank Erik Reese, Marshall Joy and Laura Grego for taking part in the observations that began this project. We acknowledge Gus Evrard for providing the hydrodynamical cluster simulations used to determine the survey sensitivity. YTL acknowledges financial support from the University of Illinois Research Board. JJM acknowledges financial support from the NASA Long Term Space Astrophysics grant NAG 5-11415.

REFERENCES

- Barbosa, D., Bartlett, J. G., Blanchard, A., & Oukbir, J. 1996, *A&A*, 314, 13
- Bryan, G. L. & Norman, M. L. 1998, *ApJ*, 495, 80
- Bunn, E. F. & White, M. 1997, *ApJ*, 480, 6
- Burles, S. & Tytler, D. 1998, *ApJ*, 507, 732
- Carlstrom, J. E., Joy, M., & Grego, L. 1996, *ApJ*, 456, L75
- Carlstrom, J. E., Joy, M. K., Grego, L., Holder, G. P., Holzzapfel, W. L., Mohr, J. J., Patel, S., & Reese, E. D. 2000, *Physica Scripta Volume T*, 85, 148
- Carroll, S. M., Press, W. H., & Turner, E. L. 1992, *ARA&A*, 30, 499
- Cavaliere, A. & Fusco-Femiano, R. 1978, *A&A*, 70, 677
- Davis, M., Efstathiou, G., Frenk, C. S., & White, S. D. M. 1985, *ApJ*, 292, 371
- Dawson, K. S., Holzzapfel, W. L., Carlstrom, J. E., Joy, M., LaRoque, S. J., & Reese, E. D. 2001, *ApJ*, 553, L1
- Dawson, K. S., Holzzapfel, W. L., Carlstrom, J. E., LaRoque, S. J., Miller, A., Nagai, D., & Joy, M. 2002, *ApJ*, submitted (astro-ph/0206012)
- Eisenstein, D. J. & Hu, W. 1998, *ApJ*, 496, 605
- Evrard, A. E. 1988, *MNRAS*, 235, 911
- . 1990, *ApJ*, 363, 349
- Fan, Z. & Chiueh, T. 2001, *ApJ*, 550, 547
- Fixsen, D. J., Cheng, E. S., Gales, J. M., Mather, J. C., Shafer, R. A., & Wright, E. L. 1996, *ApJ*, 473, 576
- Haiman, Z. ., Mohr, J. J., & Holder, G. P. 2001, *ApJ*, 553, 545
- Henry, J. P. 1997, *ApJ*, 489, L1
- Holder, G., Haiman, Z. ., & Mohr, J. J. 2001, *ApJ*, 560, L111
- Holder, G. P. & Carlstrom, J. E. 1999, in *ASP Conf. Ser.* 181: *Microwave Foregrounds*, 199
- Holder, G. P., Mohr, J. J., Carlstrom, J. E., Evrard, A. E., & Leitch, E. M. 2000, *ApJ*, 544, 629
- Holzzapfel, W. L., Carlstrom, J. E., Grego, L., Holder, G., Joy, M., & Reese, E. D. 2000a, *ApJ*, 539, 57
- Holzzapfel, W. L., Carlstrom, J. E., Grego, L., Joy, M., & Reese, E. D. 2000b, *ApJ*, 539, 67
- Hu, W. & Dodelson, S. 2001, *ARA&A*, in press (astro-ph/0110414)
- Hu, W. & Kravtsov, A. 2002, *ApJ*, submitted astro-ph/0203169
- Jenkins, A., Frenk, C. S., White, S. D. M., Colberg, J. M., Cole, S., Evrard, A. E., Couchman, H. M. P., & Yoshida, N. 2001, *MNRAS*, 321, 372
- Jones, M. E., Saunders, R., Baker, J. C., Cotter, G., Edge, A., Grainge, K., Haynes, T., Lasenby, A., Pooley, G., & Rottgering, H. 1997, *ApJ*, 479, L1
- Kneissl, R. ., Jones, M. E., Saunders, R., Eke, V. R., Lasenby, A. N., Grainge, K., & Cotter, G. 2001, *MNRAS*, 328, 783
- Lo, K. Y., Chiueh, T., Liang, H., Ma, C. P., Martin, R., Ng, K.-W., Pen, U. L., & Subramanyan, R. 2000, in *IAU Symposium*, Vol. 201
- Majumdar, S. & Subrahmanyam, R. 2000, *MNRAS*, 312, 724
- Mathiesen, B., Evrard, A. E., & Mohr, J. J. 1999, *ApJ*, 520, L21
- Mathiesen, B. F. & Evrard, A. E. 2001, *ApJ*, 546, 100
- Mohr, J. J. 2001, in *AMiBA 2001: High-z Clusters, Missing Baryons and CMB Polarization*, ASP conference series, eds. L-W Chen, C-P Ma, K-W Ng, U-L Pen, in press (astro-ph/0112502)
- Mohr, J. J. & Evrard, A. E. 1997, *ApJ*, 491, 38
- Mohr, J. J., Mathiesen, B., & Evrard, A. E. 1999, *ApJ*, 517, 627
- Mohr, J. J., Reese, E. D., Ellingson, E., Lewis, A. D., & Evrard, A. E. 2000, *ApJ*, 544, 109
- Navarro, J. F., Frenk, C. S., & White, S. D. M. 1997, *ApJ*, 490, 493
- Netterfield et al. 2001, *ApJ*, submitted (astro-ph/0104460)
- Pierpaoli, E., Scott, D., & White, M. 2001, *MNRAS*, 325, 77
- Press, W. H. & Schechter, P. 1974, *ApJ*, 187, 425
- Press, W. H., Teukolsky, S. A., Vetterling, W. T., & Flannery, B. 1992, *Numerical Recipes in C* (Cambridge: Cambridge University Press)
- Reese, E. D., Mohr, J. J., Carlstrom, J. E., Joy, M., Grego, L., Holder, G. P., Holzzapfel, W. L., Hughes, J. P., Patel, S. K., & Donahue, M. 2000, *ApJ*, 533, 38
- Richards, E. A., Fomalont, E. B., Kellerman, K. I., Partridge, R. B., & Windhorst, R. A. 1997, *AJ*, 113, 1475
- Springel, V., White, M., & Hernquist, L. 2001, *ApJ*, 549, 681
- Subrahmanyam, R., Kesteven, M. J., Ekers, R. D., Sinclair, M., & Silk, J. 2000, *MNRAS*, 315, 808
- Sunyaev, R. A. & Zeldovich, Y. B. 1970, *Ap&SS*, 7, 3
- Sunyaev, R. A. & Zel'dovich, Y. B. 1972, *Comments Astrophys. Space Phys.*, 4, 173
- Viana, P. T. P. & Liddle, A. R. 1999, *MNRAS*, 303, 535
- Weller, J., Battye, R., & Kneissl, R. 2001, *astro-ph* (0110353)

APPENDIX

Here we examine the H_0 dependence of survey sensitivity, showing how in an interferometric survey it departs significantly from the expected scaling for a flux limited survey. For an approximately virialized and self-similar cluster population, the density weighted electron temperature scales with the cluster mass: $\langle T_e \rangle \propto (Mh)^{2/3}$ (e.g. Bryan & Norman 1998; Mohr et al. 2000). Eqn 5 then implies that the galaxy cluster SZE flux scales as $S_\lambda \propto M_{200}^{5/3} h^{8/3}$. Therefore, the limiting mass in an SZE flux limited survey would scale as $M_{lim} \propto h^{-8/5}$.

In interferometric surveys, it is the cluster apparent size and morphology along with the total cluster flux that play important roles in determining the detectability of a cluster. The limiting mass is that mass which produces a particular detection significance $\Delta\chi^2$, where the detection significance scales as the cluster visibility squared. From Eqn 6 it is clear that cluster visibility is proportional to the cluster flux, so if flux were the only important factor we would expect $\Delta\chi^2 \propto M_{200}^\alpha$ with $\alpha = 10/3$. However, the best fit $\Delta\chi^2 - M_{200}$ relations exhibit significantly shallower slopes: $\alpha \sim 2.3 - 2.4 < 10/3$ (at $z = 0.5$; see Fig 1). This underscores the sensitivity of the visibility to cluster angular size and shape. At a particular redshift, increasing cluster mass means increasing total cluster flux, but this effect is partially offset by the larger cluster apparent size, which reduces the signal at any particular baseline.

There is also considerable scatter in the $\Delta\chi^2 - M_{200}$ relation. We have inspected the simulated clusters that fall well below the best fit $\Delta\chi^2 - M_{200}$ relation; these clusters generally appear more extended and irregular (in some cases bimodal). Many of these morphologically complex clusters are obviously in the midst of a major merger, and their complex shape causes diminution of the cluster visibility over the angular scales where the BIMA survey is most sensitive.

To obtain the h dependence of the interferometric survey sensitivity, we need only know the slope of the $\Delta\chi^2 - M_{200}$ relation and the h dependence of $\Delta\chi^2$ and M_{200} . At fixed ICM temperature (T_e), $M_{200} \propto h^{-1}$ and $\Delta\chi^2 \propto h^2$. Including the h dependence in the $\Delta\chi^2 - M_{200}$ relation leads to $(\Delta\chi^2 h^{-2}) \propto (M_{200} h)^\alpha$. Keeping the required detection significance $\Delta\chi^2$ fixed provides h scaling: $M_{lim} \propto h^{-(2+\alpha)/\alpha}$. For $\alpha = 10/3$ which is derived from assuming only flux is important in determining the cluster detection significance, we arrive at $M_{lim} \propto h^{-8/5}$, consistent with expectations for a flux limited survey. Taking the typical measured slope $\alpha = 2.4$, we calculate the true h sensitivity of the limiting mass to be $M_{lim} \propto h^{-11/6}$. The shallower the $\Delta\chi^2 - M_{200}$ relation, the larger shift in M_{lim} required to offset a change in h .